

SDiT: Semantic Region-Adaptive for Diffusion Transformers

Bowen Lin¹ Fanjiang Ye² Yihua Liu⁶ Zhenghui Guo¹ Boyuan Zhang³
 Weijian Zheng⁴ Yufan Xu⁵ Tiancheng Xing⁶ Yuke Wang² Chengming Zhang^{1*}

¹University of Houston ²Rice University ³Indiana University Bloomington

⁴Argonne National Laboratory ⁵National University of Singapore ⁶Independent Researcher

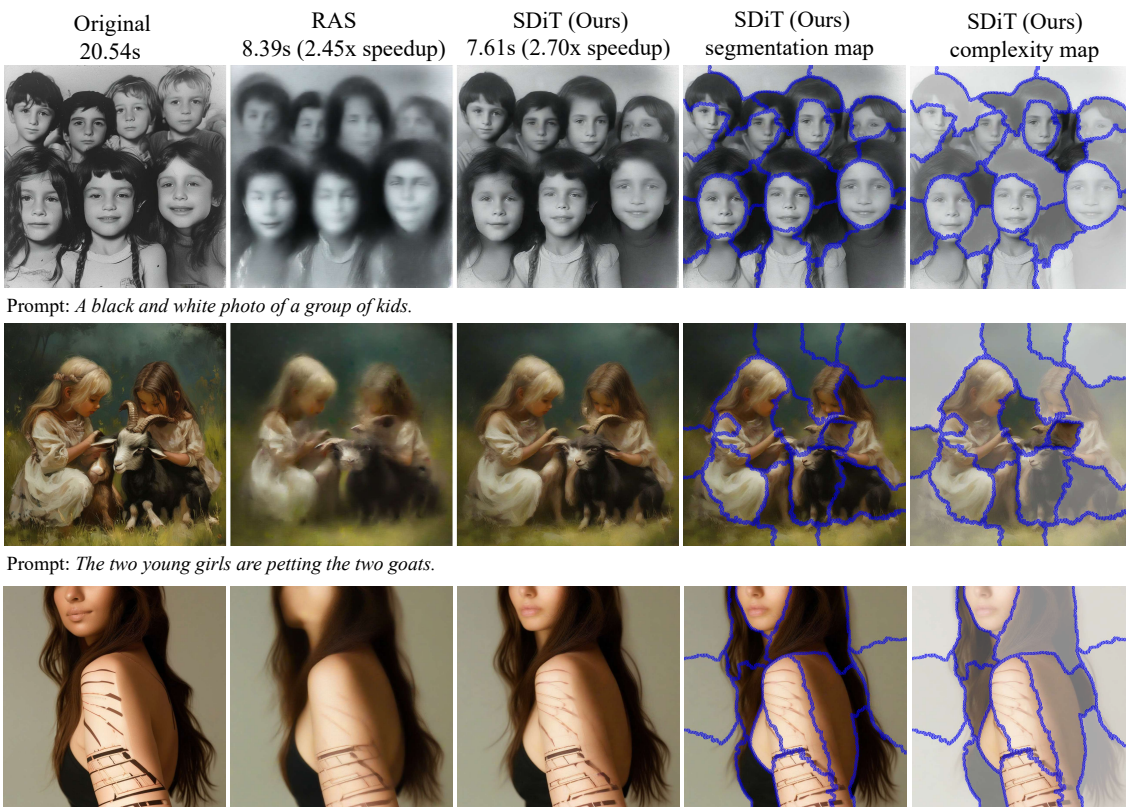


Figure 1. **SDiT accelerates image generation while maintaining high fidelity.** We introduce SDiT, a training-free algorithm that accelerates diffusion transformer inference by dynamically allocating computation across semantically coherent regions, achieving substantial speedup while preserving image fidelity. Under the same model and step budget, our method achieves a 2.70x speedup with sharp details and good boundary preservation. Even on the most challenging cases—such as single or multi-face generation, SDiT consistently preserves fine details and structural coherence. In contrast, RAS struggles to maintain pixel fidelity (e.g., blurred or collapsed facial textures) across object regions. The rightmost columns visualize SDiT’s segmentation and complexity maps which guide adaptive region-wise denoising. Setting: Lumina-Next with 30-step, 1024 × 1024 resolution. Latency is measured on Ada6000.

Abstract

Diffusion Transformers (DiTs) achieve state-of-the-art performance in text-to-image synthesis but remain computationally expensive due to the iterative nature of denoising

and the quadratic cost of global attention. In this work, we observe that denoising dynamics are spatially non-uniform—background regions converge rapidly while edges and textured areas evolve much more actively. Building on this insight, we propose SDiT, a Semantic Region-Adaptive

Diffusion Transformer that allocates computation according to regional complexity. SDiT introduces a training-free framework combining (1) semantic-aware clustering via fast Quickshift-based segmentation, (2) complexity-driven regional scheduling to selectively update informative areas, and (3) boundary-aware refinement to maintain spatial coherence. Without any model retraining or architectural modification, SDiT achieves up to 3.0 \times acceleration while preserving nearly identical perceptual and semantic quality to full-attention inference.

1. Introduction

Diffusion models [12] have achieved remarkable success in generative modeling, producing images with high fidelity and semantic coherence. Beyond static image synthesis [33], they have shown strong capability across diverse visual tasks, including image editing [9, 31], inpainting [26, 38], painting [32, 37], video synthesis [14], and 3D generation [19, 35]. Among these, Diffusion Transformers (DiTs) [33] represent the state of the art by combining the expressive power of attention [42] with diffusion-based denoising. However, the quadratic $O(n^2)$ attention cost and iterative sampling make DiTs computationally prohibitive for high-resolution or real-time generation. Achieving practical deployment thus requires efficient inference acceleration without retraining.

Recent training-free methods aim to accelerate diffusion inference with pre-trained models. DPM-Solver [24] reformulates the reverse process as an ODE and applies high-order solvers to reduce sampling steps. DistriFusion [18] improves throughput via patch-level parallelism, while Δ -DiT [5] exploits block-wise redundancy through delta-based caching. Although effective, these methods mainly reduce temporal or hardware redundancy and still process the entire feature map uniformly, ignoring spatial variation.

In practice, different image regions exhibit distinct denoising dynamics: detailed areas such as textures and boundaries evolve rapidly, while smooth backgrounds remain stable [17, 37]. Allocating equal computation to all regions, therefore wastes considerable resources. Region-Adaptive Sampling (RAS) [22] partially addresses this by assigning higher update frequency to bright color regions, but its intensity-based policy lacks semantic awareness, often leading to blurred or inconsistent results.

To address these limitations, we propose SDiT, a semantic region-adaptive diffusion framework that dynamically allocates denoising computation according to semantic structure and local complexity, enabling spatially adaptive yet globally coherent generation without retraining.

To further investigate this idea, we visualize the diffusion process at different sampling steps, as shown in Figure 2.



Figure 2. Visualization of the diffusion process

ure 2. Based on the predicted final states x_{pred}^t , we observe that as the timestep progresses, the information gain Δx_{pred}^t is primarily concentrated in textured and boundary regions. A closer examination of denoising trajectories reveals non-uniform spatial evolution: background regions exhibit stable, low-complexity dynamics, while textured and boundary areas change rapidly. However, updating only high-complexity regions leads to degraded coherence, as local attention relies on contextual continuity. Low-complexity areas, though visually simple, often provide crucial cues for adjacent high-complexity zones.

Building on these insights, SDiT integrates semantic understanding with adaptive regional computation to focus resources where they matter most. It features three key components: (1) an efficient clustering-based semantic segmentation that partitions the image into contiguous, semantically coherent regions for joint refinement and consistent global attention; (2) a region-adaptive complexity estimation mechanism that dynamically reallocates computation according to denoising progress, emphasizing high-frequency regions while reducing redundant updates in smooth areas (3) a boundary-aware enhancement module that reinforces object edges and high-frequency details to mitigate potential artifacts.

Together, these components form a unified, zero-shot region-adaptive framework that achieves substantial acceleration while preserving texture fidelity, structural coherence, and semantic consistency, all without retraining or modifying any DiT parameters.

To validate our approach, we apply SDiT on a state-of-the-art text-to-image generation DiT models LumaNext T2I [50]. Extensive experiments demonstrate clear improvements: with the same computational budget, our approach produces notably higher generation quality, with FID score improved by 14% using 8% less computation and achieves comparable fidelity while achieving up to 3.0 \times end-to-end speedup with less than 20% of FID score drop. We summarize our key contributions as follows:

- We conduct an in-depth analysis of the regional correlation of diffusion process, revealing that denoising should be based on semantic segmentation and dynamics.
- We propose SDiT, a training-free and efficient DiT inference system that dynamically updates regions based on semantic segmentation, achieving high-quality and effi-

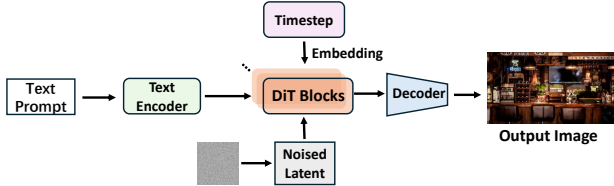


Figure 3. Overview of Diffusion Transformer Structure.

cient generation.

- SDiT delivers a significant speedup up to 3.0x while maintaining good image generation quality, paving the way for efficient image generation.

2. Related Work

2.1. Latent Diffusion Transformer Models

Latent Diffusion Models (LDMs) [13, 37, 40] have become a leading paradigm for high-fidelity image synthesis by performing diffusion in a compact latent space. An encoder \mathcal{E} first projects an input x to a latent code $z_0 = \mathcal{E}(x)$. The model then runs a two-phase stochastic process: a forward (noising) phase and a reverse (denoising) phase. In the forward phase, Gaussian noise is progressively injected into z_0 across T timesteps according to a predetermined variance schedule $\{\beta_t\}_{t=1}^T$, yielding a latent that approaches the standard normal distribution $\mathcal{N}(0, I)$, as described in Eq. 1.

$$q(\mathbf{z}_t \mid \mathbf{z}_{t-1}) = \mathcal{N} \left(\mathbf{z}_t; \sqrt{1 - \beta_t} \mathbf{z}_{t-1}, \beta_t \mathbf{I} \right). \quad (1)$$

In the reverse process, a learnable noise prediction network is utilized to reconstruct the original data z_o by iteratively denoising from the noised sample z_T , as outlined in Equation 2, where $\mu_\theta(\mathbf{z}_t, t)$ and $\Sigma_\theta(\mathbf{z}_t, t)$ are the predicted mean and variance of the Gaussian distribution.

$$p_\theta(\mathbf{z}_{t-1} \mid \mathbf{z}_t) = \mathcal{N} \left(\mathbf{z}_{t-1}; \mu_\theta(\mathbf{z}_t, t), \Sigma_\theta(\mathbf{z}_t, t) \right). \quad (2)$$

Among various diffusion backbones, the Diffusion Transformer (DiT) [4, 8, 34] has become particularly prominent due to its strong modeling capacity and scalability. Rather than preserving the original spatial resolution for pooling as in earlier convolutional U-Nets [37], DiT operates without this constraint, making it possible to mine spatial redundancy during the diffusion process. In a typical DiT-based image generation pipeline inference as shown in Figure 3, we sample Gaussian noise in the VAE latent space and feed it, together with timestamp embeddings and text features, into the DiT model, and after iterative denoising, the refined latent is decoded by the VAE to produce the final image. This design decouples computation from the fixed image grid: once positional embeddings are added, tokens can be addressed individually, enabling adaptive selection of salient tokens at each step (Sec. 1) and substantially improving diffusion efficiency [23].

2.2. Efficient Diffusion Models

Due to the high cost of inference in diffusion models, it's necessary to apply optimizations to improve the generation efficiency, commonly including both training-free and non-training-free methods.

Non-training-free methods. Many non-training-free methods aim to reduce the sampling steps. For example, the progressive distillation [47, 48] aims to train simple and few-step models. Another method, like consistency models [41], which learns a time-consistent mapping so that predictions at different noise levels agree, enabling one- or few-step generation via consistency training. What's more, the rectified flow [2, 21], which learns a vector field whose ODE follows near-straight trajectories from a base Gaussian to the data distribution, shortening transport paths and reducing the number of sampling steps.

Training-free methods. There also exist training-free approaches that reduce the number of sampling steps and the computation within each step. Methods such as DPM-solver [24, 25] refine the underlying ODE trajectories to enable fast integration. In parallel, caching has emerged as a practical way to lower per-step cost by reusing intermediate activations: early studies primarily targeted U-Net backbones [1, 28], while later efforts for DiTs explored output reuse, block skipping, and residual reuse [27, 39]. However, these techniques typically treat all image regions uniformly, overlooking spatially varying complexity. Recent work therefore allocates computation adaptively across regions [15, 22, 46], yielding substantial gains in efficiency.

3. Motivation and Analysis

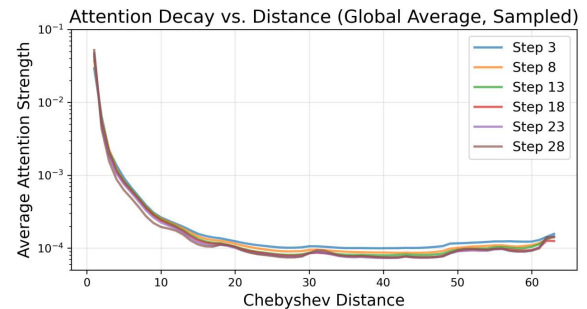


Figure 4. Average attention strength as a function of Chebyshev distance across denoising steps.

Diffusion Transformers suffer from high computational costs because each denoising step requires performing global self-attention over the entire latent feature map. A natural way to reduce this cost is to introduce **spatial sparsity**—that is, updating only a subset of regions at each timestep. However, how to divide the latent into meaningful regions while maintaining semantic coherence and attention

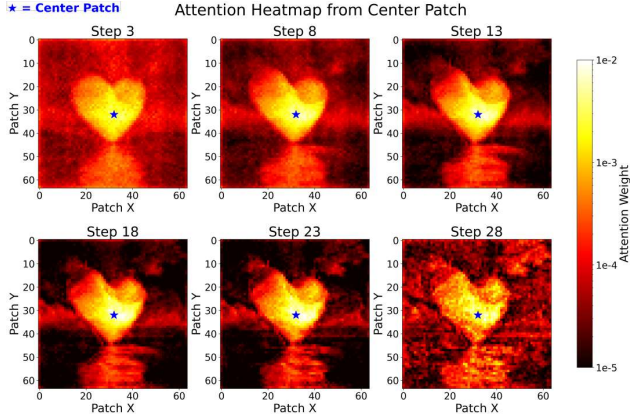


Figure 5. Attention heatmaps from the center patch (marked by a blue star) across denoising steps.

consistency remains a key challenge for efficient sparse diffusion.

3.1. Attention Observation

As shown in Figure 4 and Figure 5, the attention map from a representative center patch reveals a clear local preference: the highest attention weights are concentrated around nearby patches, while distant regions contribute minimally. This confirms that DiT’s attention mechanism primarily captures short-range spatial dependencies, reflecting an inherent locality bias in diffusion transformers.

However, a closer inspection of the heatmaps uncovers a more intriguing phenomenon: the attended regions are not randomly distributed but instead form coherent semantic clusters that align with the underlying object structure. For instance, in the example figure, the high-attention area naturally outlines the heart-shaped object and its reflection, suggesting that the model implicitly organizes attention according to semantic and structural boundaries. In other words, attention tends to follow the shape of meaningful regions rather than purely relying on Euclidean proximity.

This observation indicates that while the transformer inherently focuses on local neighborhoods, its attention also exhibits semantic grouping behavior—a property that can be leveraged to design more adaptive region-based acceleration strategies. Instead of treating all square patches equally, we can utilize this semantic prior to partition the latent space into content-aware regions that better respect object boundaries and visual coherence.

3.2. Limitations of Existing Region Division

A straightforward idea is to partition the latent variable into multiple regions and assign different computational budgets to each. Three simple strategies are commonly used:

K-Means clustering [29]: grouping pixels based on feature similarity.

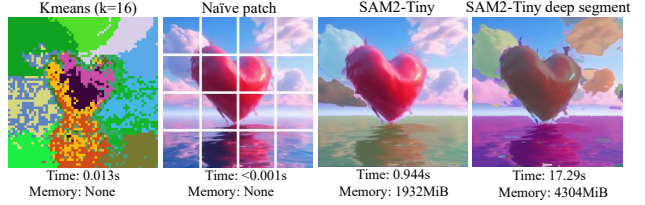


Figure 6. Comparison of different region segmenting methods

Uniform patch partition [6]: dividing the image into fixed-size blocks.

Segmentation-model division: using a pretrained semantic segmentation model to obtain region masks.

However, all of these strategies have inherent limitations.

(1) K-Means clustering groups pixels solely based on feature similarity, completely ignoring spatial adjacency. As a result, distant pixels from the same object may be assigned to different clusters, while foreground and background pixels may be mixed due to similar colors. The resulting regions are highly fragmented, spatially disconnected, and poorly aligned with semantic structures.

(2) Uniform patch partition maintains spatial continuity but disregards structural boundaries. A single patch may contain both smooth background and sharp edges, while adjacent patches belonging to the same object are treated independently. This disrupts attention dependencies across regions, leading to inconsistent updates, broken contours, and texture artifacts.

(3) Segmentation-model-based division uses pretrained models (e.g., SAM 2 [36]) to derive semantic masks, but the segmentation results often yield highly unbalanced region sizes, and require expensive inference with extra memory overhead, which hinders its use for iterative adaptive scheduling during diffusion.

Figure 6 visually compares these three strategies. As shown, none of them simultaneously achieves semantic integrity, spatial continuity, and computational efficiency.

4. Methodology

4.1. Intelligent Semantic-aware Division

As illustrated in Figure 7, given the latent variable x_t at timestep t , our goal is to divide it into semantically coherent regions, enabling different regions to be updated with distinct computational budgets.

To this end, we propose a *Quickshift-based dynamic clustering* method that integrates both denoising dynamics and spatial continuity. Specifically, we extract two latent features from the denoising network ϵ_θ : the predicted clean image x_{pred}^t and the predicted noise $\epsilon_\theta(x_t)$. For each spatial location i , we construct a feature descriptor:

$$f_i^t = [x_{\text{pred}}^t \parallel \epsilon_\theta(x_t)_i]. \quad (3)$$

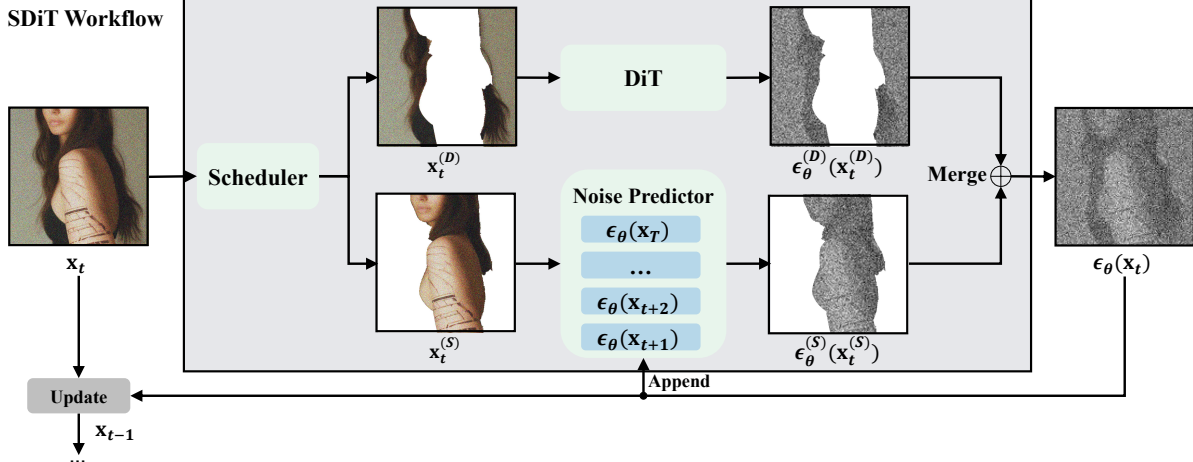


Figure 7. Dynamic region scheduling in SDiT. The input latent is first processed by a fast semantic segmentation module, where each region is treated as an independent unit for subsequent updates. The complexity estimator then computes the denoising complexity of each region, and the scheduler selects the top- k most complex regions for active denoising. To maintain spatial continuity and enhance high-frequency boundaries, boundary dilation is applied to the selected regions before merging. Finally, the latent space is divided into two types of regions—actively updated regions and momentum-based cached regions—achieving adaptive region-level denoising scheduling.

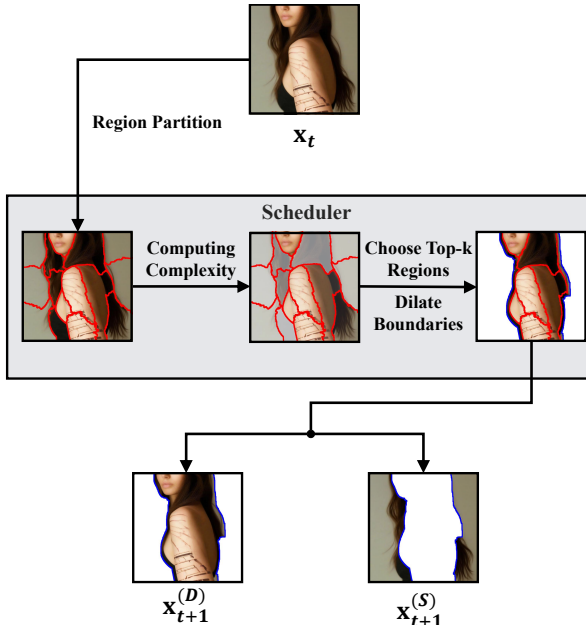


Figure 8. Overview of the SDiT Scheduler. The input latent is first processed by a fast semantic segmentation module, where each region is treated as an independent unit for subsequent updates. The complexity estimator then computes the denoising complexity of each region, and the scheduler selects the top- k most complex regions. To maintain spatial continuity and enhance high-frequency boundaries, boundary dilation is applied to the selected regions before performing active denoising.

Instead of K-Means, we apply the density-based Quickshift clustering algorithm [16, 43] with approximate nearest neighbor (ANN) acceleration [30]. Quickshift naturally enforces spatial connectivity and does not require a predefined number of clusters K , making it ideal

for dynamically evolving semantics in diffusion. With ANN acceleration, the overall complexity is reduced from $O(N^2)$ to $O(N \log N)$, and the clustering stage becomes lightweight—each clustering operation takes no more than 20 ms and accounts for less than 5% of the total inference time.

The latent space is thus partitioned into K regions:

$$\{M_1, M_2, \dots, M_K\}, \quad M_k = \{i \mid \text{Quickshift}(f_i^t) = k\}. \quad (4)$$

Here, i denotes a spatial position (i.e., pixel or patch index) in the latent feature map at timestep t , and $\text{Quickshift}(\cdot)$ represents the clustering operator that assigns each position i to one of K clusters based on its local density in the feature space. Each cluster M_k therefore corresponds to a spatially contiguous and semantically coherent region in the latent domain.

The feature descriptor combines two complementary components: (1) the predicted clean latent x_{pred}^t encoding semantic content, and (2) the noise prediction $\epsilon_\theta(x_t)$ encoding denoising dynamics. This joint representation ensures that clustering reflects both spatial semantics and temporal denoising behavior.

Each region M_k serves as the basic scheduling unit for selective denoising, re-computed each step to follow evolving semantics while preserving global context and temporal coherence.

4.2. Efficient Region-aware Scheduling

Figure 8 shows the workflow of SDiT scheduler. After obtaining semantic regions $M_{k=1, \dots, K}$, the key challenge becomes determining which regions to update, when to update them, and how to update them without breaking spatial co-

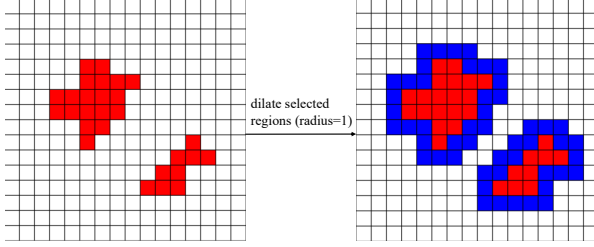


Figure 9. Process of dilating boundary

herence. We propose an efficient regional scheduling strategy composed of three components: complexity-based selection, boundary-aware refinement, and velocity-space extrapolation.

Complexity-Based Region Selection. For each spatial location i , we define a lightweight complexity score that reflects the local denoising difficulty:

$$C_i^t = \frac{1}{C} \sum_{c=1}^C \left[\underbrace{\alpha \sqrt{(\partial_x x_{\text{pred},i,c}^t)^2 + (\partial_y x_{\text{pred},i,c}^t)^2}}_{\text{edge / texture}} + \underbrace{\gamma |\Delta x_{\text{pred},i,c}^t|}_{\text{fine details}} + \underbrace{\beta |x_{i,c}^t - x_{\text{pred},i,c}^t|}_{\text{residual noise}} \right] \quad (5)$$

Here, x_t and x_{pred}^t denote the noisy and predicted clean latents, i and c are spatial and channel indices, ∂_x, ∂_y are spatial gradients, and Δ is the Laplacian operator. α, γ, β control the weighting of edges, fine structures, and residual noise.

Instead of averaging complexity over all pixels in a region—which would dilute sharp structures with smooth areas—we compute the mean of the top $q\%$ complex pixels within each region:

$$\bar{C}_k^t = \frac{1}{|\text{Top}_q(M_k)|} \sum_{i \in \text{Top}_q(M_k)} C_i^t \quad (6)$$

Regions are ranked by \bar{C}_k^t , and only the top $p(t)$ regions are selected for denoising at timestep t . The rest reuse cached predictions from the previous step.

Boundary-aware Refinement. Updating only selected regions may cause boundary artifacts because attention becomes asymmetric across region borders. As shown in Figure 9, to ensure consistent updates, we apply an 8-connected dilation to each selected region:

$$M_k^{\text{ext}} = \text{Dilate}(M_k, r = 1) \quad (7)$$

and define the full update set as:

$$\Omega_t = \bigcup_{k \in \text{Top-}p(t)} M_k^{\text{ext}} \quad (8)$$

This boundary expansion ensures both sides are updated, preserving contour continuity and semantic consistency.

Non-Uniform Velocity Space Extrapolation. Low complexity regions change more gradually during denoising, showing greater temporal stability and more reliable predictability than highly dynamic areas. Taking advantage of this property, we model their latent evolution and predict the next-step noise from previous timesteps, which greatly reduces computational cost. However, the diffusion schedule $\{\epsilon_t\}$ is non-uniform, causing the scale of $\epsilon_\theta(x_t, t)$ to vary with the step interval. To achieve consistent modeling across irregular steps, we perform extrapolation in the *velocity space*, defined as

$$v_t = \frac{\epsilon_\theta(x_t, t)}{\sigma_t - \sigma_{t-1}}, \quad (9)$$

where σ_t denotes the noise standard deviation at step t . Given observed pairs $\{(\sigma_i, v_i)\}_{i=0}^t$, we estimate v_{t+1} via Newton interpolation with recursively defined divided differences:

$$\begin{aligned} v[\sigma_i] &= v_i, \\ v[\sigma_i, \sigma_{i+1}] &= \frac{v_{i+1} - v_i}{\sigma_{i+1} - \sigma_i}, \\ v[\sigma_i, \dots, \sigma_{i+k}] &= \frac{v[\sigma_{i+1}, \dots, \sigma_{i+k}] - v[\sigma_i, \dots, \sigma_{i+k-1}]}{\sigma_{i+k} - \sigma_i}. \end{aligned} \quad (10)$$

We define the Newton basis term as

$$\alpha_k(\sigma_{t+1}) := \prod_{j=0}^{k-1} (\sigma_{t+1} - \sigma_{t-j}), \quad \alpha_0 \equiv 1, \quad (11)$$

and introduce a k -dependent decay weight to attenuate higher-order terms over large temporal gaps:

$$w_k = \exp[-\lambda(\sigma_t - \sigma_{t-k})]. \quad (12)$$

The extrapolated velocity is then given by

$$v_{t+1} \approx \sum_{k=0}^n w_k \alpha_k(\sigma_{t+1}) v[\sigma_{t-k}, \dots, \sigma_t]. \quad (13)$$

Finally, we convert the result back to the noise space as

$$\hat{\epsilon}_{t+1} = v_{t+1} \cdot (\sigma_{t+1} - \sigma_t), \quad (14)$$

which provides temporally consistent and scale-normalized noise estimates for stable or skipped regions under non-uniform schedules.

4.3. Other Quality Optimizations

Dynamic Sampling Ratio. We divide the denoising process into three perceptual phases—(1) structure formation, (2) stable refinement, and (3) detail restoration—and design

a cosine-based Structure–Stable–Detail (SSD) scheduling to match these dynamics:

$$p(t) = \begin{cases} p_{\max}, & \frac{t}{T} < \tau_1, \\ p_{\min} + \frac{p_{\max}-p_{\min}}{2} \left(1 + \cos \left(\pi \cdot \frac{\frac{t}{T} - \tau_1}{\tau_2 - \tau_1} \right) \right) & \tau_1 \leq \frac{t}{T} \leq \tau_2, \\ p_{\max}, & \frac{t}{T} > \tau_2, \end{cases} \quad (15)$$

where $\tau_1 \approx 0.1$ and $\tau_2 \approx 0.95$.

Global Refresh Steps. To prevent long-term drift in sparse updates, we insert several full-image denoising steps at critical moments: (1) Warm-up: early steps where clustering is unstable; (2) Cool-down: late steps for recovering fine details; (3) Error reset: when cached predictions diverge significantly.

These steps incur negligible overhead, substantially enhancing temporal stability and perceptual consistency.

5. Experiment

5.1. Setup

Models. We evaluate our method on a state-of-the-art, open-sourced diffusion transformer models based on the flow matching paradigm: Lumina-Next T2I. This model generates images in latent space and employs transformer-based architectures with cross-frame self-attention.

Metrics. We evaluate both efficiency and generation quality of accelerated sampling. For fidelity, we report Fréchet Inception Distance [11] (FID, lower is better) computed against ground-truth images as well as the original full-step diffusion outputs. To measure reconstruction consistency with the original model, we use PSNR and SSIM [45] (higher is better) and LPIPS [49] (lower is better), which together capture pixel-level accuracy, structural similarity, and perceptual alignment. To measure text-image alignment, we use CLIP score [10]. Efficiency is assessed using latency per image (s/image) and the corresponding speedup ratio relative to full sampling.

Datasets. We evaluate our method on two complementary text–image datasets to cover both real-world and synthetic generation scenarios. From MS-COCO 2017 dataset [20], we sample 5,000 caption–image pairs and use the captions to generate images at 1024×1024 resolution, testing semantic alignment and realism in natural scenes. From the Human Preference Synthetic Dataset (DALLE3 1M+ HQC) [7], which is generated by DALLE3 [3] and CogVLM [44], we sample another 5,000 pairs with challenging prompts and detail-rich images to assess performance in creative and imaginative settings.

Baselines. We compare our approach with the existing region-based strategy for accelerating diffusion transformer

Method	Steps	Ratio	time (s)	FID (↓)	CLIP (↑)
MS-COCO 2017					
Original	10	1	7.39	37.12	21.23
SDiT	14	0.5	6.89	35.85	21.51
Original	5	1	4.09	92.19	18.91
SDiT	7	0.5	3.74	76.60	20.29
Dalle3 1M+ HQC					
Original	10	1	7.31	51.48	29.66
SDiT	14	0.5	6.84	49.90	30.07
Original	5	1	4.01	107.30	23.84
SDiT	7	0.5	3.69	93.95	26.22

Table 1. Performance comparison under different steps and sampling ratios.

inference. Region-Adaptive Sampling (RAS) selects regions with high noise magnitude or residual error—often corresponding to areas of high color saturation or brightness. RAS denoises these patches while reusing the output of the last diffusion process for other patches.

5.2. Efficiency Evaluation

As shown in Table 5.2, SDiT delivers a stable and predictable trade-off between quality and speed as the sampling ratio decreases. Instead of a sudden degradation, visual fidelity declines smoothly, indicating that the model adapts gracefully to reduced computation. At moderate ratios (around 0.5–0.6), the overall perceptual quality remains close to full sampling, with FID and CLIP scores nearly unchanged and structural metrics (PSNR, SSIM) showing only minor loss.

Even when the sampling ratio is pushed to 0.125, SDiT achieves nearly 3× faster inference on the MS-COCO 2017 dataset while preserving coherent structures and consistent semantics. This demonstrates that a large fraction of denoising updates can be safely skipped without compromising perceptual realism.

More importantly, SDiT exhibits remarkable fidelity under the Original Image Comparison metrics, showing that its sparse updates remain highly faithful to the original image. The reconstruction error is significantly lower than RAS, and the FID score is reduced by more than half with slightly higher acceleration rates. This suggests that SDiT performs sparse sampling in a more structured and semantically aligned way, producing results that are visually closer to full inference while achieving substantially higher efficiency.

5.3. Quality Evaluation

In Table 5.1, our method maintains lower wall-clock time than full-attention sampling while achieving consistently lower FID and visually more accurate results. On the MS-COCO 2017 dataset, SDiT attains 1.1× acceleration (4.09 s → 3.74 s) and 15.6 lower FID compared with the baseline. This demonstrates that uniformly updating every patch is

Method	Steps	Ratio	Time (s)	Speedup	G.T. Comparison		Original Image Comparison			
					FID (↓)	CLIP (↑)	FID (↓)	PSNR (↑)	SSIM (↑)	LPIPS (↓)
Original	30	1	23.72	-	29.63	21.52	-	-	-	-
RAS	30	0.5	13.92	1.7x	32.67	21.68	11.74	22.57	0.73	0.26
	30	0.25	10.31	2.3x	39.25	21.78	20.82	21.23	0.68	0.24
	30	0.125	8.10	2.93x	41.95	21.91	23.52	20.97	0.66	0.27
SDiT	30	0.5	14.32	1.66x	30.03	21.59	4.78	25.96	0.85	0.12
	30	0.25	10.29	2.31x	31.62	21.65	8.18	23.37	0.77	0.13
	30	0.125	7.91	3.0x	35.50	21.84	14.23	21.85	0.71	0.20
Original	10	1	7.31	-	51.48	29.66	-	-	-	-
RAS	10	0.65	6.03	1.22x	70.34	28.49	19.26	25.03	0.76	0.17
	10	0.45	5.44	1.34x	84.07	27.21	30.38	23.84	0.72	0.21
	10	0.25	4.30	1.70x	104.43	25.19	49.22	23.06	0.69	0.26
SDiT	10	0.6	5.80	1.26x	60.41	29.06	8.78	27.72	0.84	0.09
	10	0.4	4.81	1.52x	69.34	28.32	14.13	25.84	0.79	0.14
	10	0.2	3.72	1.97x	91.41	26.22	31.85	23.69	0.73	0.24

Table 2. Performance comparison across different methods on MS-COCO 2017 dataset.

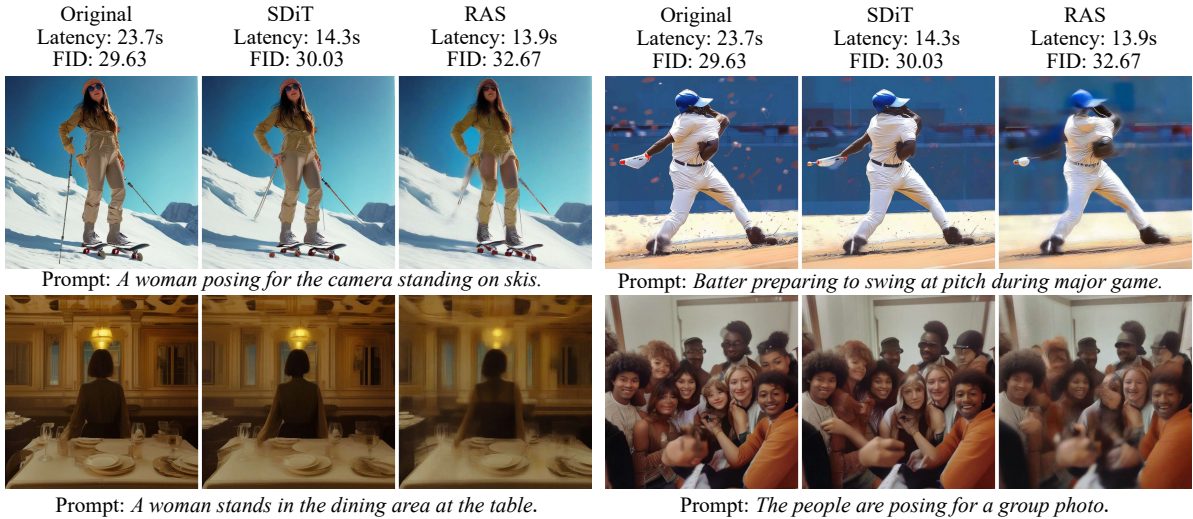


Figure 10. Qualitative results. Evaluated by FID against ground truth, SDiT reduces inference latency proportionally to the sampling rate, yet preserves fine-grained details and even removes artifacts that appear in full-sampling method.

not an efficient use of computation. By concentrating denoising on structurally and semantically important regions, our approach utilizes the available budget more effectively, leading to improved perceptual quality and closer alignment with the true data distribution. In short, full attention is no longer the upper bound of quality at a fixed cost—our strategy offers a more principled and effective way to allocate computation in diffusion transformers.

6. Conclusion

In this work, we explored how semantic and structural properties within the latent space of diffusion transform-

ers can be leveraged to achieve efficient and adaptive inference. We found that different regions of an image evolve at highly uneven rates during the denoising process, and that attention patterns tend to cluster along coherent semantic boundaries. Building on these observations, we introduced SDiT, a training-free, semantic region-adaptive framework that dynamically partitions latent representations into coherent regions and allocates computation according to their local complexity. By combining semantic clustering, complexity-aware scheduling, and boundary refinement, SDiT achieves up to 3.0x acceleration while maintaining perceptual and structural quality close to full

inference, and surpasses uniform baselines under less computational budgets. Beyond efficiency, SDiT also offers a new perspective on the internal dynamics of diffusion transformers, revealing how spatial semantics and attention structures can be exploited for adaptive computation. We hope this direction inspires further exploration toward resource-efficient, structure-aware generative modeling.

References

- [1] Shubham Agarwal, Subrata Mitra, Sarthak Chakraborty, Srikrishna Karanam, Koyel Mukherjee, and Shiv Kumar Saini. Approximate caching for efficiently serving Text-to-Image diffusion models. In *21st USENIX Symposium on Networked Systems Design and Implementation (NSDI 24)*, pages 1173–1189, Santa Clara, CA, 2024. USENIX Association. [3](#)
- [2] Michael S. Albergo and Eric Vanden-Eijnden. Building normalizing flows with stochastic interpolants, 2023. [3](#)
- [3] James Betker, Gabriel Goh, Li Jing, Tim Brooks, Jianfeng Wang, Linjie Li, Long Ouyang, Juntang Zhuang, Joyce Lee, Yufei Guo, et al. Improving image generation with better captions. *Computer Science*. <https://cdn.openai.com/papers/dall-e-3.pdf>, 2(3):8, 2023. [7](#)
- [4] Junsong Chen, Jincheng Yu, Chongjian Ge, Lewei Yao, Enze Xie, Yue Wu, Zhongdao Wang, James Kwok, Ping Luo, Huchuan Lu, and Zhenguo Li. Pixart- α : Fast training of diffusion transformer for photorealistic text-to-image synthesis, 2023. [3](#)
- [5] Pengtao Chen, Mingzhu Shen, Peng Ye, Jianjian Cao, Chongjun Tu, Christos-Savvas Bouganis, Yiren Zhao, and Tao Chen. δ -dit: A training-free acceleration method tailored for diffusion transformers. *arXiv preprint arXiv:2406.01125*, 2024. [2](#)
- [6] Alexey Dosovitskiy. An image is worth 16x16 words: Transformers for image recognition at scale. *arXiv preprint arXiv:2010.11929*, 2020. [4](#)
- [7] Ben Egan, Alex Redden, XWAVE, and SilentAntagonist. Dalle3 1 Million+ High Quality Captions, 2024. [7](#)
- [8] Patrick Esser, Sumith Kulal, Andreas Blattmann, Rahim Entezari, Jonas Müller, Harry Saini, Yam Levi, Dominik Lorenz, Axel Sauer, Frederic Boesel, et al. Scaling rectified flow transformers for high-resolution image synthesis. In *Forty-first international conference on machine learning*, 2024. [3](#)
- [9] Amir Hertz, Ron Mokady, Jay Tenenbaum, Kfir Aberman, Yael Pritch, and Daniel Cohen-Or. Prompt-to-prompt image editing with cross attention control, 2022. [2](#)
- [10] Jack Hessel, Ari Holtzman, Maxwell Forbes, Ronan Le Bras, and Yejin Choi. Clipscore: A reference-free evaluation metric for image captioning. In *Proceedings of the 2021 conference on empirical methods in natural language processing*, pages 7514–7528, 2021. [7](#)
- [11] Martin Heusel, Hubert Ramsauer, Thomas Unterthiner, Bernhard Nessler, and Sepp Hochreiter. Gans trained by a two time-scale update rule converge to a local nash equilibrium. *Advances in neural information processing systems*, 30, 2017. [7](#)
- [12] Jonathan Ho, Ajay Jain, and Pieter Abbeel. Denoising diffusion probabilistic models. *Advances in neural information processing systems*, 33:6840–6851, 2020. [2](#)
- [13] Jonathan Ho, Ajay Jain, and Pieter Abbeel. Denoising diffusion probabilistic models, 2020. [3](#)
- [14] Jonathan Ho, Tim Salimans, Alexey Gritsenko, William Chan, Mohammad Norouzi, and David J. Fleet. Video diffusion models, 2022. [2](#)

[15] Wongi Jeong, Kyungryeol Lee, Hoigi Seo, and Se Young Chun. Upsample what matters: Region-adaptive latent sampling for accelerated diffusion transformers, 2025. 3

[16] Heinrich Jiang, Jennifer Jang, and Samory Kpotufe. Quick-shift++: Provably good initializations for sample-based mean shift. In *International conference on machine learning*, pages 2294–2303. PMLR, 2018. 5

[17] Sora Kim, Sungho Suh, and Minsik Lee. Rad: Region-aware diffusion models for image inpainting, 2024. 2

[18] Muyang Li, Tianle Cai, Jiaxin Cao, Qinsheng Zhang, Han Cai, Junjie Bai, Yangqing Jia, Kai Li, and Song Han. Distri-fusion: Distributed parallel inference for high-resolution diffusion models. In *Proceedings of the IEEE/CVF Conference on Computer Vision and Pattern Recognition*, pages 7183–7193, 2024. 2

[19] Chen-Hsuan Lin, Jun Gao, Luming Tang, Towaki Takikawa, Xiaohui Zeng, Xun Huang, Karsten Kreis, Sanja Fidler, Ming-Yu Liu, and Tsung-Yi Lin. Magic3d: High-resolution text-to-3d content creation, 2023. 2

[20] Tsung-Yi Lin, Michael Maire, Serge Belongie, James Hays, Pietro Perona, Deva Ramanan, Piotr Dollár, and C Lawrence Zitnick. Microsoft coco: Common objects in context. In *European conference on computer vision*, pages 740–755. Springer, 2014. 7

[21] Yaron Lipman, Ricky T. Q. Chen, Heli Ben-Hamu, Maximilian Nickel, and Matt Le. Flow matching for generative modeling, 2023. 3

[22] Ziming Liu, Yifan Yang, Chengruidong Zhang, Yiqi Zhang, Lili Qiu, Yang You, and Yuqing Yang. Region-adaptive sampling for diffusion transformers. *arXiv preprint arXiv:2502.10389*, 2025. 2, 3

[23] Ziming Liu, Yifan Yang, Chengruidong Zhang, Yiqi Zhang, Lili Qiu, Yang You, and Yuqing Yang. Region-adaptive sampling for diffusion transformers, 2025. 3

[24] Cheng Lu, Yuhao Zhou, Fan Bao, Jianfei Chen, Chongxuan Li, and Jun Zhu. Dpm-solver: A fast ode solver for diffusion probabilistic model sampling in around 10 steps. *Advances in neural information processing systems*, 35:5775–5787, 2022. 2, 3

[25] Cheng Lu, Yuhao Zhou, Fan Bao, Jianfei Chen, Chongxuan Li, and Jun Zhu. Dpm-solver++: Fast solver for guided sampling of diffusion probabilistic models. *Machine Intelligence Research*, 22(4):730–751, 2025. 3

[26] Andreas Lugmayr, Martin Danelljan, Andres Romero, Fisher Yu, Radu Timofte, and Luc Van Gool. Repaint: Inpainting using denoising diffusion probabilistic models, 2022. 2

[27] Zhengyao Lv, Chenyang Si, Junhao Song, Zhenyu Yang, Yu Qiao, Ziwei Liu, and Kwan-Yee K. Wong. Fastercache: Training-free video diffusion model acceleration with high quality, 2025. 3

[28] Xinyin Ma, Gongfan Fang, and Xinchao Wang. Deepcache: Accelerating diffusion models for free, 2023. 3

[29] J MacQueen. Multivariate observations. In *Proceedings of the 5th Berkeley Symposium on Mathematical Statistics and Probability*, pages 281–297, 1967. 4

[30] Yu A Malkov and Dmitry A Yashunin. Efficient and robust approximate nearest neighbor search using hierarchical nav-igable small world graphs. *IEEE transactions on pattern analysis and machine intelligence*, 42(4):824–836, 2018. 5

[31] Chenlin Meng, Yutong He, Yang Song, Jiaming Song, Jiajun Wu, Jun-Yan Zhu, and Stefano Ermon. Sdedit: Guided image synthesis and editing with stochastic differential equations, 2022. 2

[32] Alex Nichol, Prafulla Dhariwal, Aditya Ramesh, Pranav Shyam, Pamela Mishkin, Bob McGrew, Ilya Sutskever, and Mark Chen. Glide: Towards photorealistic image generation and editing with text-guided diffusion models, 2022. 2

[33] William Peebles and Saining Xie. Scalable diffusion models with transformers. In *Proceedings of the IEEE/CVF international conference on computer vision*, pages 4195–4205, 2023. 2

[34] William Peebles and Saining Xie. Scalable diffusion models with transformers, 2023. 3

[35] Ben Poole, Ajay Jain, Jonathan T. Barron, and Ben Mildenhall. Dreamfusion: Text-to-3d using 2d diffusion, 2022. 2

[36] Nikhila Ravi, Valentin Gabeur, Yuan-Ting Hu, Ronghang Hu, Chaitanya Ryali, Tengyu Ma, Haitham Khedr, Roman Rädle, Chloe Rolland, Laura Gustafson, Eric Mintun, Junting Pan, Kalyan Vasudev Alwala, Nicolas Carion, Chao-Yuan Wu, Ross Girshick, Piotr Dollár, and Christoph Feichtenhofer. Sam 2: Segment anything in images and videos. *arXiv preprint arXiv:2408.00714*, 2024. 4

[37] Robin Rombach, Andreas Blattmann, Dominik Lorenz, Patrick Esser, and Björn Ommer. High-resolution image synthesis with latent diffusion models, 2022. 2, 3

[38] Chitwan Saharia, William Chan, Huiwen Chang, Chris A. Lee, Jonathan Ho, Tim Salimans, David J. Fleet, and Mohammad Norouzi. Palette: Image-to-image diffusion models, 2022. 2

[39] Pratheba Selvaraju, Tianyu Ding, Tianyi Chen, Ilya Zharkov, and Luming Liang. Fora: Fast-forward caching in diffusion transformer acceleration, 2024. 3

[40] Jiaming Song, Chenlin Meng, and Stefano Ermon. Denoising diffusion implicit models, 2022. 3

[41] Yang Song, Prafulla Dhariwal, Mark Chen, and Ilya Sutskever. Consistency models, 2023. 3

[42] Ashish Vaswani, Noam Shazeer, Niki Parmar, Jakob Uszkoreit, Llion Jones, Aidan N Gomez, Łukasz Kaiser, and Illia Polosukhin. Attention is all you need. *Advances in neural information processing systems*, 30, 2017. 2

[43] Andrea Vedaldi and Stefano Soatto. Quick shift and kernel methods for mode seeking. In *European conference on computer vision*, pages 705–718. Springer, 2008. 5

[44] Weihan Wang, Qingsong Lv, Wenmeng Yu, Wenyi Hong, Ji Qi, Yan Wang, Junhui Ji, Zhuoyi Yang, Lei Zhao, Song XiXuan, et al. Cogvilm: Visual expert for pretrained language models. *Advances in Neural Information Processing Systems*, 37:121475–121499, 2024. 7

[45] Zhou Wang. Image quality assessment: from error visibility to structural similarity. *IEEE transactions on image processing*, 13(4):600–612, 2004. 7

[46] Fanjiang Ye, Zepeng Zhao, Yi Mu, Jucheng Shen, Renjie Li, Kaijian Wang, Desen Sun, Saurabh Agarwal, Myungjin Lee,

Triston Cao, Aditya Akella, Arvind Krishnamurthy, T. S. Eugene Ng, Zhengzhong Tu, and Yuke Wang. Supergen: An efficient ultra-high-resolution video generation system with sketching and tiling, 2025. [3](#)

[47] Tianwei Yin, Michaël Gharbi, Taesung Park, Richard Zhang, Eli Shechtman, Fredo Durand, and Bill Freeman. Improved distribution matching distillation for fast image synthesis. *Advances in neural information processing systems*, 37:47455–47487, 2024. [3](#)

[48] Tianwei Yin, Michaël Gharbi, Richard Zhang, Eli Shechtman, Fredo Durand, William T Freeman, and Taesung Park. One-step diffusion with distribution matching distillation. In *Proceedings of the IEEE/CVF conference on computer vision and pattern recognition*, pages 6613–6623, 2024. [3](#)

[49] Richard Zhang, Phillip Isola, Alexei A Efros, Eli Shechtman, and Oliver Wang. The unreasonable effectiveness of deep features as a perceptual metric. In *Proceedings of the IEEE conference on computer vision and pattern recognition*, pages 586–595, 2018. [7](#)

[50] Le Zhuo, Ruoyi Du, Han Xiao, Yangguang Li, Dongyang Liu, Rongjie Huang, Wenze Liu, Xiangyang Zhu, Fu-Yun Wang, Zhanyu Ma, et al. Lumina-next: Making lumina-t2x stronger and faster with next-dit. *Advances in Neural Information Processing Systems*, 37:131278–131315, 2024. [2](#)

A. Additional Ablation Studies

This appendix provides extended analyses that complement the main paper. Unless otherwise stated, all experiments are conducted on the MS-COCO 2017 dataset at 1024×1024 resolution using a Lumina_Next backbone. Sampling steps are fixed to 10 and the sampling ratio to 0.2 by default.

A.1. Region Partitioning Ablation

We first examine how different region-partitioning strategies affect the performance of SDiT. All variants operate under identical sampling ratios and scheduling rules to ensure a fair comparison. As shown in Table 3, semantic clustering-based partitioning (Quickshift, SLIC) consistently outperforms naive grid- or patch-based alternatives due to better alignment with semantic boundaries.

A.2. Complexity Score Ablation

We further study how different complexity metrics affect the selection of top- k regions. As shown in Table 4, our hybrid gradient-noise metric achieves the best performance, indicating the importance of capturing both structural and stochastic variations.

A.3. Sensitivity to Sampling Ratio and Dilation

We evaluate the joint effect of sampling ratio and dilation. As seen in Table 5, moderate dilation ($d = 1$ or $d = 2$) consistently yields better results, especially under aggressive sub-sampling, highlighting the importance of boundary coherence.

A.4. Number of Regions K

We vary the quickshift hyper-parameters to change the average number of regions. As shown in Table 6, increasing region granularity helps until segmentation becomes overly fragmented.

A.5. Quality Curve Across Sampling Steps

We evaluate sampling steps $\{3, 5, 7, 10, 15, 30\}$. As shown in Table 7, SDiT provides the largest gains at low-step regimes, where spatial complexity is highly uneven. As steps increase, the denoising trajectory becomes smoother and the advantage naturally narrows.

B. Additional Qualitative Results

We provide qualitative comparisons under different sampling ratios and sampling steps.

We further include complete quantitative comparisons on MS-COCO 2017 and DALLE3 1M+ HQC datasets for both 30-step and 10-step settings.

Table 3. Comparison of region partitioning strategies (10 steps, ratio 0.2).

Method	Compute Time	$FID \downarrow$	$FID_{ori} \downarrow$
Quickshift	0.111	83.542	51.683
SLIC	0.057	86.274	53.105
K-means	0.251	108.435	81.177
Uniform patch	0.378	91.981	58.740
Direct patch	2.251	126.250	99.418

Table 4. Ablation on complexity score metrics (10 steps, ratio 0.2).

Complexity Score	$FID \downarrow$	$FID_{ori} \downarrow$
ℓ_2 -norm	94.503	60.912
Noise amplitude	96.020	62.630
Ours	80.676	47.701
Standard deviation	94.155	60.914

Table 5. Sensitivity to sampling ratio under different dilation settings.

Dilation	Ratio	Compute (%)	$FID \downarrow$	$FID_{ori} \downarrow$
0	0.2	15.97	94.211	61.905
	0.4	36.15	59.436	26.380
	0.6	56.36	44.963	11.741
	0.8	77.84	39.739	6.645
1	0.2	21.30	80.676	47.701
	0.4	43.76	50.828	17.718
	0.6	63.77	42.144	9.334
	0.8	83.04	38.549	5.297
2	0.2	25.52	71.807	38.857
	0.4	49.45	47.149	14.484
	0.6	69.56	40.410	7.992
	0.8	87.02	37.748	4.252
3	0.2	29.42	65.709	32.679
	0.4	54.35	44.496	12.051
	0.6	74.49	39.486	6.865
	0.8	89.97	37.432	3.281
full	1	100	37.122	/

Table 6. Comparison of clustering configurations.

Average_K	Cluster	FID \downarrow	FID $_{\text{ori}}\downarrow$
11.650	0.164	97.884	65.136
22.380	0.107	95.174	62.747
30.580	0.098	94.916	62.690
58.510	0.097	94.913	63.043
76.310	0.093	94.692	62.934

Table 7. Quality comparison across sampling steps.

Method	Step	Rate	Time	FID \downarrow
Full	3	1	2.436	248.653
Full	5	1	3.824	92.192
Full	7	1	5.280	51.753
Full	10	1	7.393	37.122
Full	15	1	10.962	31.512
Full	30	1	23.724	29.627
SDiT	5	0.3	2.359	127.136
SDiT	7	0.5	3.721	76.601
SDiT	10	0.5	5.208	44.882
SDiT	14	0.5	6.885	35.855
SDiT	20	0.6	11.036	31.026
SDiT	40	0.6	21.805	29.814

Table 8. Performance comparison on MS-COCO 2017 under step=30 and step=10.

Method	Step	Rate	Cluster	Time	FID \downarrow	FID_ori \downarrow	PSNR \uparrow	SSIM \uparrow	LPIPS \downarrow
Step = 30									
Lumina_Next	30	1	/	23.724	29.627	/	/	/	/
RAS	30	0.5	/	13.924	32.666	11.738	22.566	0.732	0.260
SDiT	30	0.5	0.363	14.324	30.031	4.775	25.957	0.850	0.120
RAS	30	0.25	/	10.308	39.248	20.816	21.226	0.677	0.243
SDiT	30	0.25	0.348	10.293	31.617	8.184	23.366	0.774	0.125
RAS	30	0.125	/	8.095	41.945	23.522	20.973	0.661	0.270
SDiT	30	0.125	0.366	7.907	35.500	14.228	21.851	0.709	0.196
Step = 10									
Lumina_Next	10	1	/	7.393	37.122	/	/	/	/
RAS	10	0.65	/	6.170	54.340	21.269	24.404	0.742	0.184
SDiT	10	0.6	0.104	5.615	42.562	8.788	24.969	0.773	0.157
RAS	10	0.45	/	5.453	70.265	36.854	23.297	0.705	0.235
SDiT	10	0.4	0.112	4.892	49.639	13.705	25.214	0.775	0.148
RAS	10	0.25	/	4.295	93.314	60.050	22.605	0.677	0.284
SDiT	10	0.2	0.114	3.821	73.800	35.137	23.258	0.710	0.247

Table 9. Performance comparison on DALLE3 1M+ HQC dataset under step=30 and step=10.

Method	Step	Rate	Cluster	Time	FID \downarrow	FID_ori \downarrow	PSNR \uparrow	SSIM \uparrow	LPIPS \downarrow
Step = 30									
Lumina_Next	30	1	/	22.253	27.514	/	/	/	/
RAS	30	0.5	/	13.904	41.725	15.575	22.603	0.724	0.167
SDiT	30	0.5	0.341	14.466	31.088	5.586	26.242	0.852	0.062
RAS	30	0.25	/	10.288	50.783	22.810	21.541	0.679	0.228
SDiT	30	0.25	0.309	11.185	37.129	10.578	23.529	0.772	0.126
RAS	30	0.125	/	8.100	59.052	29.850	20.915	0.649	0.281
SDiT	30	0.125	0.358	8.456	47.269	18.786	21.889	0.703	0.202
Step = 10									
Lumina_Next	10	1	/	7.309	51.480	/	/	/	/
RAS	10	0.65	/	6.032	70.339	19.259	25.028	0.760	0.165
SDiT	10	0.6	0.109	5.798	60.411	8.781	27.718	0.840	0.090
RAS	10	0.45	/	5.442	84.073	30.377	23.843	0.724	0.214
SDiT	10	0.4	0.104	4.809	69.340	14.134	25.845	0.794	0.140
RAS	10	0.25	/	4.301	104.433	49.221	23.058	0.694	0.263
SDiT	10	0.2	0.105	3.717	91.414	31.850	23.693	0.727	0.240

Full sampling
Latency: 7.309s

Sample ratio: 0.6
Latency: 5.798s

Sample ratio: 0.4
Latency: 4.809s

Sample ratio: 0.2
Latency: 3.717s

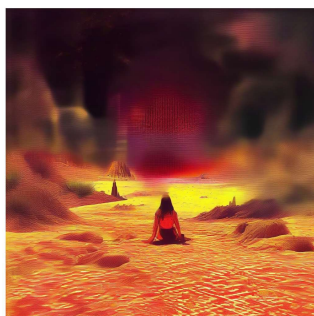
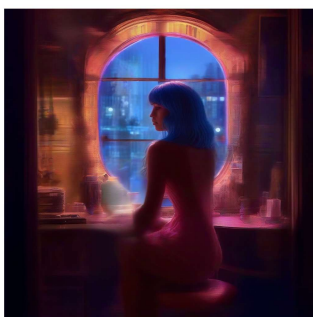
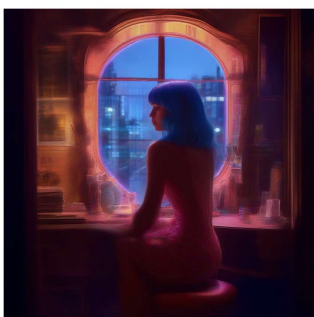


Figure 11. Qualitative comparison under 10 sampling steps. ¹⁵

Full sampling
Latency: 22.25s



Sample ratio: 0.5
Latency: 14.47s



Sample ratio: 0.25
Latency: 11.19s



Sample ratio: 0.125
Latency: 8.46s



Figure 12. Qualitative comparison under 30 sampling steps.